

Phases and magnetization process of an anisotropic Shastry-Sutherland model

Zi Yang Meng and Stefan Wessel

Institut für Theoretische Physik III, Universität Stuttgart, Pfaffenwaldring 57, 70550 Stuttgart, Germany

We examine ground state properties of the spin-1/2 easy-axis Heisenberg model on the Shastry-Sutherland lattice with ferromagnetic transverse spin exchange using quantum Monte Carlo and degenerate perturbation theory. For vanishing transverse exchange, the model reduces to an antiferromagnetic Ising model that besides Néel order harbors regions of extensive ground state degeneracy. In the quantum regime, we find a dimerized phase of triplet states, separated from the Néel ordered phase by a superfluid. The quantum phase transitions between these phases are characterized. The magnetization process shows a magnetization plateau at 1/3 of the saturation value, that persists down to the Ising limit, and a further plateau at 1/2 only in the quantum regime. For both plateaus, we determine the crystalline patterns of the localized triplet excitations. No further plateaus nor supersolid phases are found in this model.

PACS numbers: 05.30.Jp, 75.10.Jm, 71.27.+a, 75.40.Mg

I. INTRODUCTION

Quantum magnets exhibit a wealth of interesting phenomena, in particular on low-dimensional frustrated lattices, where both enhanced quantum fluctuations and geometric frustration can destroy semi-classical magnetic order. Indeed, various compounds have been characterized to provide realizations of the above paradigm. Recent examples include the valence bond solids found in $(\text{C}_2\text{H}_5)(\text{CH}_3)_3\text{P}[\text{Pd}(\text{dmit})_2]_2$ ¹ and $\text{Zn}_x\text{Cu}_{4-x}(\text{OD})_6\text{Cl}_2$ ². Another material, that has been intensively studied is $\text{SrCuB}_2(\text{BO}_3)_2$ (we refer to Ref. 3 for a detailed review of the various experimental and theoretical explorations on this system). This compound is described well by the dimer singlet ground state proven exactly previously by Shastry and Sutherland to exist⁴ in the spin-1/2 Heisenberg model on the orthogonal dimer lattice, shown in Fig. 1. Recently, new results on the magnetization process of $\text{SrCuB}_2(\text{BO}_3)_2$ have been presented. In particular, magnetization plateaus at 1/5, 1/6, 1/7, 1/9, and 2/9 of the saturated magnetization have been reported⁵, in addition to the previously established plateaus at 1/8, 1/4 and 1/3. While the existence of some of the reported plateaus is at the moment controversial⁶, new B¹¹ NMR data⁷ and magnetic torque measurements⁶ provide evidence in favor of a persistent crystalline structure of magnetic excitations also above the 1/8 plateau. The presence of intra-dimer Dzyaloshinskii-Moriya interactions in $\text{SrCuB}_2(\text{BO}_3)_2$ however calls for a more complex scenario than a direct interpretation in terms of supersolidity of triplet excitations in this regime⁶.

As another realization of the Shastry-Sutherland geometry the rare earth tetraborid TmB_4 ^{8,9} has recently been studied in finite magnetic fields. In contrast to $\text{SrCuB}_2(\text{BO}_3)_2$, this metallic compound exhibits stable long-range antiferromagnetic order in zero field below about 9.8 K. Since full saturation can be obtained for magnetic fields parallel to the c-axis above 5T, TmB_4 allows for a complete scan of its magnetization process. For this compound magnetization plateaus have been observed e.g. at fractions 1/2, 1/7, 1/8 and 1/9 of mag-

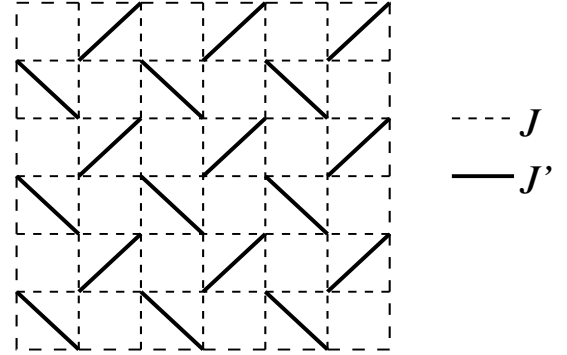


FIG. 1: The orthogonal dimer lattice of the Shastry-Sutherland model with spin-1/2 degrees of freedom on the square lattice vertices, and intra-dimer coupling J' (solid lines) and nearest neighbor (inter-dimer) coupling J (dashed lines).

netic saturation. Despite the metallic nature of TmB_4 , its magnetism has been suggested to realize an easy-axis anisotropic version of the Shastry-Sutherland model close to the Ising limit with similar intra- and inter-dimer coupling strengths⁹.

In light of the progress in realizing novel quantum phases in frustrated quantum magnets, it is important to explore in detail the interplay between geometric frustration and quantum fluctuations in such systems based on effective spin models. In many aspects, numerical studies have become especially important as an unbiased approach to quantum magnetism. However, numerical studies of even simple models of frustrated spin systems suffer from severe restrictions on the finite sizes accessible to current simulation techniques. In particular, quantum Monte Carlo (QMC) simulations are hampered by a notorious sign-problem¹⁰ due to odd-length spin-exchange paths appearing on non-bipartite lattices. This usually restricts unbiased numerical studies to the small lattices accessible to exact numerical diagonalization. Noteworthy in this respect are however recent studies employing the density matrix renormalization group algorithm on

the triangular and kagome lattice Heisenberg model^{11,12}.

Here, we employ a different approach in order to explore the interplay between quantum fluctuations and frustration, by studying a model of quantum magnetism in a parameter regime, where geometric frustration is restricted to the classical sector, and does not lead to QMC sign problems. This allows us to employ large-scale QMC simulations to study quantum effects on a frustrated spin system. In particular, we study the ground state properties of the spin-1/2 easy-axis Heisenberg model on the orthogonal dimer lattice considered by Shastry and Sutherland⁴. Namely, we consider the XXZ Hamiltonian

$$H = J \sum_{\langle i,j \rangle} [-\Delta(S_i^x S_j^x + S_i^y S_j^y) + S_i^z S_j^z] + J' \sum_{\langle\langle i,j \rangle\rangle} [-\Delta(S_i^x S_j^x + S_i^y S_j^y) + S_i^z S_j^z], \quad (1)$$

a variant of the model considered in Ref. 4 with ferromagnetic transverse exchange ($\Delta > 0$) and antiferromagnetic Ising exchange interactions $J, J' \geq 0$. Here, \mathbf{S}_i denotes a spin-1/2 degree of freedom on site i of the square lattice, and the first sum extends over all nearest neighbor bonds. The second sum runs over a staggered subset of the next-nearest neighbor bonds, as indicated in Fig. 1.

The model in Eq. (1) maintains the frustrated nature of the antiferromagnetic Ising interactions, and introduces ferromagnetic spin exchange terms. Employing the well known mapping between spin-1/2 degrees of freedom and hard-core bosons, the model can be mapped onto an extended bosonic Hubbard model of hard-core bosons hopping along the bonds of the Shastry-Sutherland lattice and experiencing repulsive interactions proportional to the strength of the Ising exchange. Recently, similar hard-core boson models have been studied on different lattice geometries, and were found to exhibit interesting order-by-disorder phenomena when quantum fluctuations lift an extensive ground state degeneracy from the Ising limit $\Delta = 0$, with new quantum phases emerging. Examples include a supersolid phase on the triangular lattice^{13,14,15,16}, valence-bond-solids^{17,18} and a Z_2 spin liquid^{19,20,21} on the kagome lattice, and a $U(1)$ liquid on the pyrochlore lattice²². In the limit of dominating kinetic terms, such models stabilize a superfluid phase on both bipartite and non-bipartite lattices. In magnetic language, the superfluid corresponds to a transverse ferromagnetic spin alignment, driven by the ferromagnetic nature of the transverse spin exchange. For the remainder of the paper, we prefer using the spin language, but occasionally find it convenient to also employ the bosonic notation.

As reviewed in the following section, the antiferromagnetic Ising model on the Shastry-Sutherland lattice exhibits regions of extensive ground state degeneracy, similar to the Ising model on the triangular and kagome lattices. Motivated by the above mentioned studies on these frustrated geometries, we here assess the effects of quantum fluctuations on the classical degenerate ground states on the Shastry-Sutherland lattice, and explore the phase diagram of the full quantum model. We find in

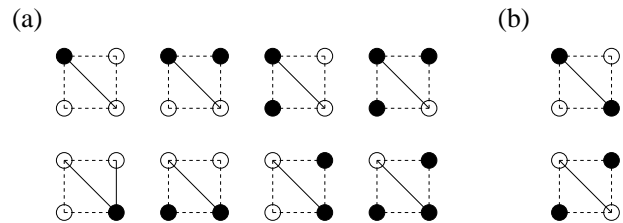


FIG. 2: (a) Possible spin configurations in the Ising limit on a non-void plaquette for $J' > 2J$. (b) Additional configurations allowed on a non-void plaquette at $J' = 2J$. Full (open) circles denote spin up (down) states.

this system a dimer triplet state, discussed in detail below, to emerge out of the classical degenerate region. In addition, the system shows a Néel ordered phase and a superfluid regime. We study the quantum phase transitions between these different phases, and consider the effects of a magnetic field. We do not obtain indications for supersolidity in this model, but find that quantum effects lead to the stabilization of a magnetization plateau at 1/2 of the full saturation, that does not persist down to the Ising limit. This is in contrast to the case of e.g. the triangular and kagome lattice, where all plateaus found in the quantum regime persist down to the Ising limit, where they have a largest extension.

The remainder of the paper is organized as follows: In the next section, we review the properties of the antiferromagnetic Ising model on the Shastry-Sutherland lattice. Then, we present in Sec. III our numerical results on the phase diagram of the model introduced above. In order to explain in a simple picture the emergence of the dimer triplet phase, we employ degenerate perturbation theory around the Ising limit, which will be discussed in Sec. IV. In Sec. V, we analyze the properties of the system in finite magnetic fields, discuss the appearing magnetization plateaus, and scan for supersolid phases. Finally, we conclude in Sec. VI by relating our numerical finding to the properties of the isotropic Heisenberg antiferromagnet ($\Delta = -1$) on the Shastry-Sutherland lattice, and discuss connections to recent studies on its magnetization process. We also comment on the recent work on the compound TmB_4 , suggested to realize the easy-axis antiferromagnetic Shastry-Sutherland model close to the Ising limit ($-1 \ll \Delta < 0$)⁹.

II. ISING LIMIT

Before exploring in detail the phase diagram of the quantum spin model introduced above, it is convenient to review the properties of the Ising limit, $\Delta = 0$, discussed in Ref. 4. In the Ising limit, the model in Eq. (1) stabilizes an antiferromagnetic Néel phase for sufficiently weak J' , up to $J'/J < 2$. For $J' > 2J$ the classical system has a macroscopically degenerate ground state manifold with an extensive ground state entropy

$S = [\ln(2)/2]k_B N = 0.347k_B N$, from all configurations that cover each of the J' dimer bonds with a pair of opposite spins. Here, N denotes the number of spins. Exactly for $J' = 2J$, the degeneracy of the ground state manifold is further enlarged, as additional low-energy configurations proliferate. Shastry and Sutherland proved a lower bound $S \geq 0.4812 k_B N$ on the ground state entropy at $J' = 2J$, via mapping the model to a 10-vertex model and using brading techniques⁴. A simple estimate of the ground state degeneracy can be obtained by employing the argument from Pauling's estimate of the residual entropy of ice²³. For this purpose, consider one of the filled plaquettes on the Shastry-Sutherland lattice. While for $J' > 2J$ the eight configurations shown in Fig. 2 (a) provide minimal contributions of this plaquette to the total energy, for $J' = 2J$ the two configurations shown in Fig. 2 (b) also lead to a minimal energy contribution. Given that out of the 16 possible configurations of the four spins forming the plaquette these 10 configurations are thus feasible, we obtain an estimate for the ground state entropy

$$S \approx k_B \ln \left[2^N \left(\frac{10}{16} \right)^{N/2} \right] = 0.458 k_B N, \quad (2)$$

to be compared to the above bound by Shastry and Sutherland. We note, that for $J' > 2J$ the Pauling estimate $S = k_B \ln(2^{N/2})$ recovers the exact result.

Besides the Ising limit, Shastry and Sutherland considered the effects of antiferromagnetic transverse spin exchange terms ($\Delta < 0$ in our notation), and proved that the system possesses an exact dimer-singlet product eigenstate, that at least for $J' > 2J$ becomes the system's ground state⁴. Later studies by various groups considered the full quantum phase diagram of this model, which up to date is not conclusively established (c.f. Ref. 3 for a review of the various theoretical and numerical proposals), even though numerical evidence has been put forward, that the $SU(2)$ symmetric model ($\Delta = -1$) features indeed three phases: (i) a low- J' antiferromagnetically ordered Néel phase, (ii) the large- J' dimer singlet phase, and (iii) an intermediate valence bond crystal (VBC) phase, which breaks the lattice symmetry by forming resonating plaquette singlet states on one of the subsets of the void plaquettes of the Shastry-Sutherland lattice²⁴. This VBC phase has a two-fold degenerate ground state and a finite spin excitation gap. For the remainder of this work, we study the quantum model in the region $\Delta > 0$, where large-scale QMC simulations are possible, in contrast to the previously studied case of $\Delta < 0$. Furthermore, this model relates directly to a model of hard-core bosons, as mentioned in Sec. I.

III. QUANTUM PHASE DIAGRAM

In this section, we present our numerical results on the phase diagram of the model in Eq. (1). These results are

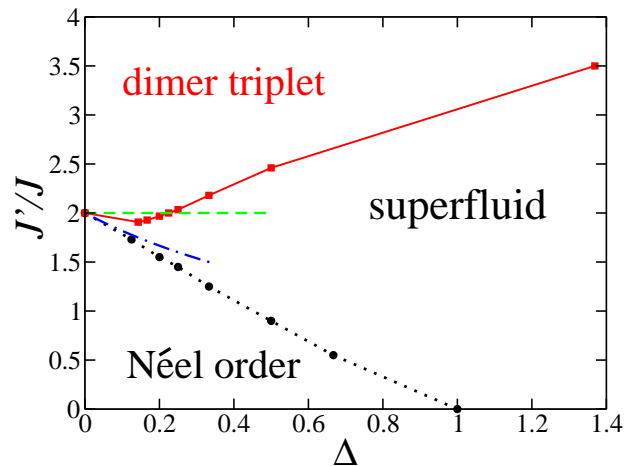


FIG. 3: (Color online) Ground state phase diagram of the spin-1/2 XXZ model on the Shastry-Sutherland lattice with ferromagnetic transverse spin exchange. The dotted (solid) line denotes a first-order (continuous) quantum phase transition. Uncertainties on the indicated phase boundaries are below the symbol size. The dashed line is a guide to the eye indicating a line of constant $J'/J = 2$. The dashed-dotted line gives the estimated phase boundary of the dimer triplet phase within perturbation theory around the point $(J'/J, \Delta) = (2, 0)$, discussed in Sec. IV.

based on QMC simulations of finite systems with up to $N = 36 \times 36$ lattice sites, using periodic boundary conditions. In the simulations, we scaled the inverse temperature as $\beta = 1/T = 8L/\Delta J$ in order to access ground state properties. Here, L denotes the linear system size. The QMC simulations were performed employing a generalized directed-loop update^{25,26} in the stochastic series expansion (SSE) algorithm²⁷. For the results obtained on the larger lattices, in particular in finite magnetic fields, we employed a decoupling of the Hamiltonian in plaquette terms, instead of the more conventional bond decoupling for the SSE formulation.

In Fig. 3, we present the ground state phase diagram resulting from our calculations. We find that the extent of the antiferromagnetically ordered Néel phase shrinks essentially linearly upon increasing Δ from 0 up to the Heisenberg point at $(\Delta, J'/J) = (1, 0)$ (for $J' = 0$, the model reduces to a spin model on the bipartite square lattice, and the sign of Δ can be inverted by a unitary transformation, thus relating the point $(\Delta, J'/J) = (1, 0)$ to the isotropic Heisenberg model at $(\Delta, J'/J) = (-1, 0)$). In hard-core bosonic language, the Néel phase corresponds to a checkerboard solid with alternating occupation of the lattice sites. In our QMC simulations, we determine the corresponding structure factor S_{AF} for antiferromagnetic order,

$$S_{AF} = \frac{1}{N} \sum_{i,j} \epsilon_i \epsilon_j \langle S_i^z S_j^z \rangle \quad (3)$$

where $\epsilon_i = \pm 1$, depending on the sublattice, to which lattice site i belongs. Néel order is present, if in the ther-

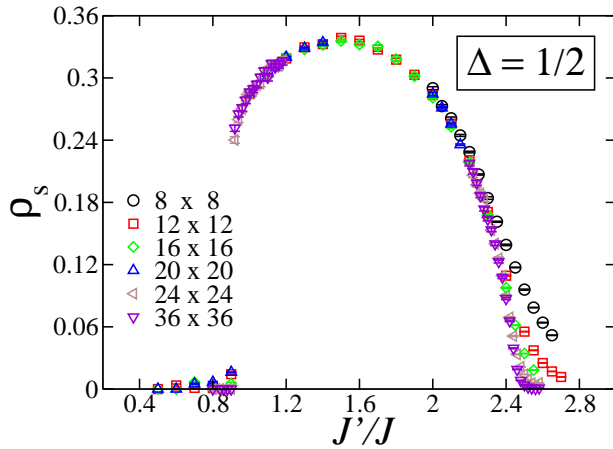


FIG. 4: (Color online) Spin stiffness ρ_S at fixed $\Delta = 1/2$ as a function of J'/J for different system sizes.

modynamic limit S_{AF}/N scales to a finite value. For dominant transverse exchange, $\Delta \gg 1$, the model reduces to an ferromagnetic XY model on the Shastry-Sutherland lattice, which in bosonic language relates to an non-frustrated tight-binding hopping model. Hence, the system is expected to exhibit a bosonic superfluid phase for large values of $\Delta > 0$, which in spin language relates to a ferromagnetic ordering within the XY plane. Such a phase is characterized by a finite value of the superfluid density, or spin stiffness, which in the QMC simulations can be obtained from measuring the spin winding number fluctuation²⁸ $\langle W^2 \rangle$ as

$$\rho_S = \frac{T}{\Delta J} \langle W^2 \rangle. \quad (4)$$

As an example, we show in Fig. 4 the behavior of ρ_S for different system sizes as a function of J'/J for fixed $\Delta = 1/2$. A region with finite spin stiffness is found for $0.9 \lesssim J'/J \lesssim 2.5$. The strong discontinuity of ρ_S at $J'/J = 0.9$ indicates that the quantum phase transition between the Néel ordered phase and the superfluid is strongly first order. Such behavior is also seen by monitoring the antiferromagnetic structure factor S_{AF} upon crossing the phase boundary, as shown in Fig. 5, again for $\Delta = 1/2$. Combining the results for S_{AF} and ρ_S , we obtain no indication for an intermediate region exhibiting both finite superfluidity and diagonal long-range order as inside a supersolid phase, as expected from the commensurate half-filling of the lattice. For dominant J' (e.g., $J'/J > 2.5$ at $\Delta = 1/2$), both S_{AF} and ρ_S eventually vanish. We explicitly verified that inside this regime the model does not exhibit long-ranged correlations in the longitudinal nor the transverse spin-spin correlation function. In addition, also the bond-order-wave structure factors do not exhibit long-ranged order in the spin exchange correlation function (corresponding to kinetic energy correlations in the bosonic model).

Since the parameter region with $J' > 2J$ approaches the degenerate region of the Ising limit for $\Delta \rightarrow 0$, quan-

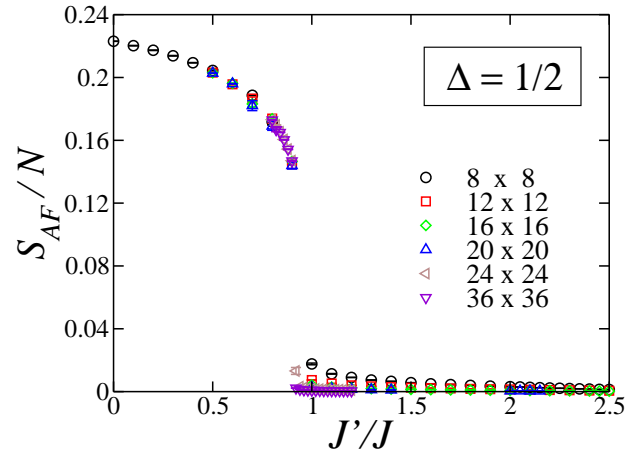


FIG. 5: (Color online) Antiferromagnetic structure factor across the phase boundary between the Néel ordered phase and the superfluid regime at fixed $\Delta = 1/2$ as a function of J'/J for different system sizes.

tum effects indeed select a unique phase from this degenerate ground state manifold. In particular, for small values of $\Delta \ll 1$, the ground state in this large- J' regime can be obtained using degenerate perturbation theory around the Ising limit, discussed in detail in the next section. Within first-order perturbation theory in Δ one then finds that for $J' > 2J$ quantum fluctuations select the following dimerized state of localized $S_{tot}^z = 0$ triplet states on each dimer:

$$|\psi_D\rangle = \bigotimes_d \frac{1}{\sqrt{2}} (|\uparrow\downarrow\rangle + |\downarrow\uparrow\rangle)_d. \quad (5)$$

Here, the direct product extends over all J' dimer bonds on the lattice. Obviously, this symmetric linear local combination results from the ferromagnetic nature of the transverse spin exchange ($\Delta > 0$) considered here. For $\Delta < 0$, one instead recovered the exact dimer singlet state found by Shastry and Sutherland⁴. In contrast to the dimer singlet state however, the above state $|\psi_D\rangle$ is not an eigenstate of the Hamiltonian for finite values of J . As discussed in the following sections, processes in higher order perturbation theory lead to local correlations between the dominant resonances on the dimers. Hence, the ground state in the large- J' region of the quantum phase diagram does not take the above direct product form, but approaches it for $J/J' \rightarrow 0$. From the ground state energy, we still find that the state $|\psi_D\rangle$ provides a appropriate variational state for the true ground state in the large- J' regime. This can be seen even at $\Delta = 1/2$, i.e. significantly away from the Ising limit, from a comparison between the system's ground state energy E and the variational energy of $|\psi_D\rangle$,

$$E_D = \langle \psi_D | H | \psi_D \rangle = -\frac{NJ'}{8} (1 + 2\Delta), \quad (6)$$

shown in Fig. 6. Due to the dominant formation of

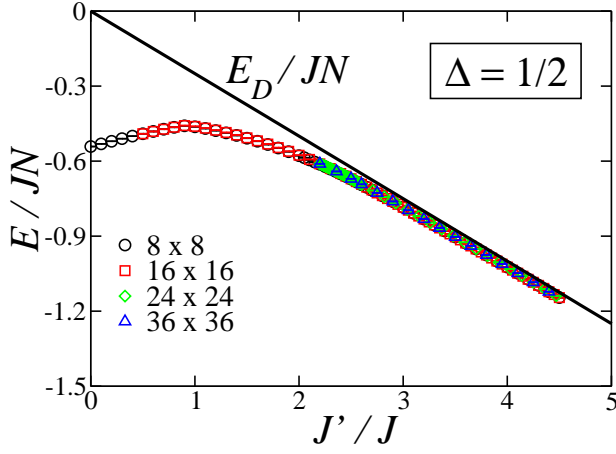


FIG. 6: (Color online) Comparison of the ground state energy E as a function of J'/J for $\Delta = 1/2$ and the variational energy of the dimerized state of localized $S_{tot}^z = 0$ triplet states, $E_D = \langle \psi_D | H | \psi_D \rangle$.

$S_{tot}^z = 0$ triplet states on the dimer bonds, we denote this magnetically disordered phase as a dimer triplet phase.

Since no spatial symmetry is broken in the dimer triplet phase, we expect the quantum phase transition from the superfluid with broken $U(1)$ symmetry to the dimer triplet phase to be continuous, and to belong in the universality class of the three-dimensional (3D) $O(2)$ model, with a dynamical critical exponent $z = 1$. In order to study the nature of this quantum phase transition in the QMC simulations, we scanned the transition region at fixed values of either Δ or J'/J , varying the other parameter through the phase boundary. Denoting the varied parameter by X , at a continuous quantum phase transition the spin stiffness scales as

$$\rho_S(X, L) = L^{-z} f(t_X L^{1/\nu}, \beta/L^z) \quad (7)$$

with a scaling function f , and the correlations length exponent ν . Here,

$$t_X = \frac{X - X_c}{X_c} \quad (8)$$

denotes the relative distance away from the critical point at $X = X_c$. From the above scaling relation, it follows that X_c can be determined as the crossing point of finite size data for the rescaled spin stiffness $L^z \rho_S$. Furthermore, with appropriate values of the critical exponents z and ν , the scaling function $f(\cdot, A)$ is then obtained by plotting $L^z \rho_S$ vs. $t_X L^{1/\nu}$ for a fixed value of $\beta/L^z = A$. As an example, we consider a scan in $X = J'/J$ at a fixed value of $\Delta = 1/2$, for which the finite size data of ρ_S is shown in Fig 7 (a). For $z = 1$, we obtain $X_c = 2.46(2)$ from a clear crossing point in Fig 7 (b), and a clear data collapse within a finite critical region, taking $\nu = 0.6723$ for the 3D $O(2)$ model²⁹, as shown in Fig. 7 (c).

Proceeding this way for other values of Δ , we eventually obtained the phase boundary shown in Fig. 3. From

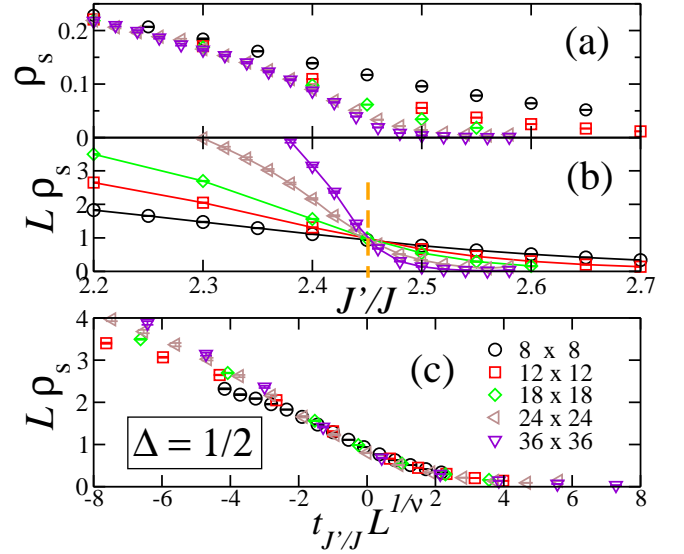


FIG. 7: (Color online) Spin stiffness ρ_S at fixed $\Delta = 1/2$ as a function of J'/J for different system sizes (a), and rescaled with linear system size L (b), with $J'/J = 2.46$ marked by the dashed line. Part (c) shows the data collapse expected from a finite size scaling analysis for the 3D $O(2)$ universality class.

this analysis, we find that at low values of $\Delta \lesssim 0.225$, the dimer triplet phase extends below the line $J'/J = 2$, indicated by the dashed line in Fig. 3. In order to illustrate this explicitly, we show in the left panels of Fig. 8 the results of the finite size scaling analysis at $\Delta = 1/6$, where the transition point is located at $J'/J = 1.928(5) < 2$. As a crosscheck, the right panel of Fig. 8 shows the data of the finite size scaling analysis at fixed $J'/J = 1.928$, where the transition is indeed observed at $\Delta = 1/6$. Similarly, when varying Δ at fixed $J'/J = 2$ a transition point between the dimer triplet phase and the superfluid regime is found at $\Delta = 0.225(1)$, as extracted from Fig. 9. These results suggest that either (i) the superfluid region separating the Néel ordered phase and the dimer triplet phase persists down to the Ising limit, or (ii) the first order transition line and the second order transition line meet at a finite value of Δ , or (iii) an additional phase appears near $J' = 2J$ for even smaller values of $\Delta < 0.1$.

Such an additional phase might be expected to be selected by quantum effects from the state of enlarged degeneracy of the Ising model at $J' = 2J$ for finite Δ . The QMC simulations could not be extended to significantly smaller values of Δ , due to an reduced efficiency in parameter regions dominated by the frustrated diagonal part of the Hamiltonian. However, as discussed in the following section, degenerate perturbation theory in Δ indicates that at $J' = 2J$ the dominant effect of a finite Δ is to effectively drive the system away from $J' = 2J$ towards the region $J' > 2J$. This leads us to exclude option (iii) from the above list. Scenario (ii) would imply a direct first order transition between the Néel ordered phase and the dimer triplet state for sufficiently low val-

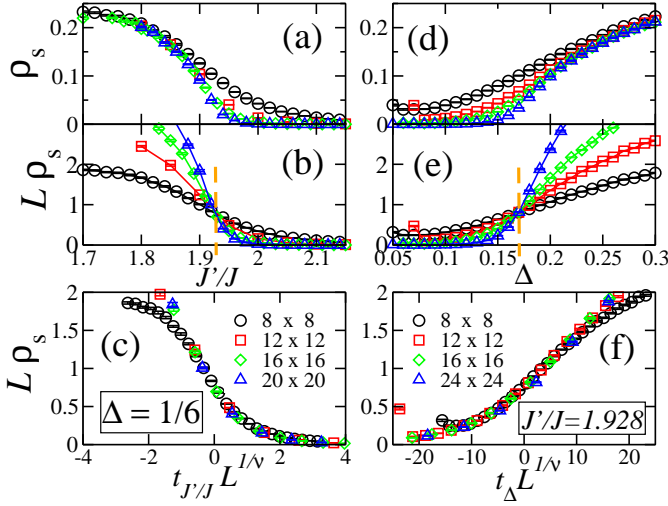


FIG. 8: (Color online) Left panel: Spin stiffness ρ_s at fixed $\Delta = 1/6$ as a function of J'/J for different system sizes (a), and rescaled with linear system size L (b), with $J'/J = 1.928$ marked by the dashed line. Part (c) shows the data collapse for the 3D $O(2)$ universality class. Right panel: Spin stiffness ρ_s at fixed $J'/J = 1.928$ as a function of Δ for different system sizes (d), and rescaled with linear system size L (e), with $\Delta = 1/6$ marked by the dashed line. Part (f) shows the data collapse for the 3D $O(2)$ universality class.

ues of $\Delta > 0$, whereas within scenario (i) the superfluid phase would always separate the two phases.

IV. PERTURBATION THEORY

In order to study more closely the emergence of the dimer triplet phase from the Ising limit upon introducing transverse exchange interactions, we employed degenerate perturbation theory, starting from the degenerate ground state manifold in the Ising limit $\Delta = 0$. First, we consider the region $J' > 2J$, where the degenerate ground state manifold is spanned by independently placing two opposite spins on each J' -dimer, as discussed in Sec. II.

For each such J' -dimer d , we denote these two lowest energy states as

$$\begin{aligned} |\Downarrow\rangle_d &= |\uparrow\downarrow\rangle_d, \\ |\Uparrow\rangle_d &= |\downarrow\uparrow\rangle_d, \end{aligned} \quad (9)$$

which form an effective spin-1/2 degree of freedom on the dimer d . We separate the full Hilbert space of the system into the model space M , spanned by these ground state configurations, and the orthogonal space O . A basis of M is given by the orthonormal states

$$|\psi_a\rangle = \bigotimes_d |\psi_a\rangle_d, \text{ with } |\psi_a\rangle_d \in \{|\Downarrow\rangle_d, |\Uparrow\rangle_d\}. \quad (10)$$

The orthogonal space O is spanned by all states of the Ising model, that do not belong to this set. We denote

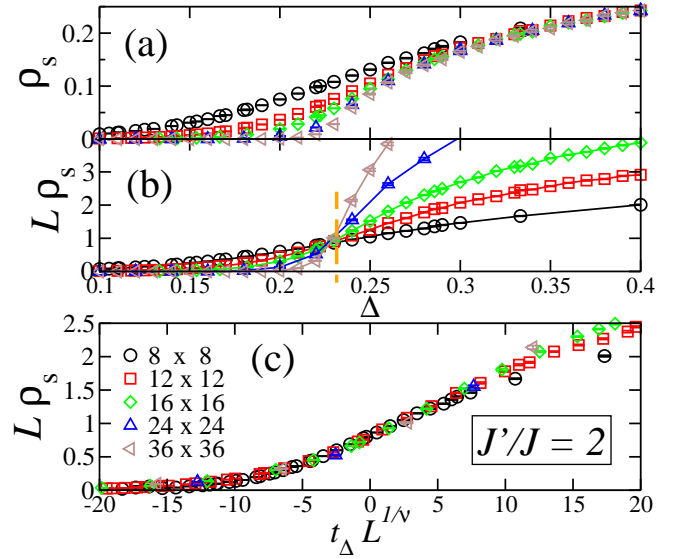


FIG. 9: (Color online) Spin stiffness ρ_s at fixed $J'/J = 2$ as a function of Δ for different system sizes (a), and rescaled with linear system size L (b), with $\Delta = 0.225$ marked by the dashed line. Part (c) shows the data collapse expected from a finite size scaling analysis for the 3D $O(2)$ universality class.

these orthonormal basis states by $|\psi_b\rangle$, for which at least one dimer d has both spins equal, i.e. $|\Uparrow\rangle_d$ or $|\Downarrow\rangle_d$. The Hamiltonian of Eq. (1) is similarly split into the model Hamiltonian H_0 and a perturbation part $H_1 \propto \Delta$,

$$\begin{aligned} H_0 &= J \sum_{\langle i,j \rangle} S_i^z S_j^z + J' \sum_{\langle\langle i,j \rangle\rangle} S_i^z S_j^z; \\ H_1 &= J \sum_{\langle i,j \rangle} [-\Delta(S_i^x S_j^x + S_i^y S_j^y)] \\ &\quad + J' \sum_{\langle\langle i,j \rangle\rangle} [-\Delta(S_i^x S_j^x + S_i^y S_j^y)], \end{aligned} \quad (11)$$

where H_0 is diagonal in the basis of M and O introduced above. The effective Hamiltonian H_{eff} , that describes the effective dynamics induced by H_1 within the model space M is given by degenerate perturbation theory up to third order in Δ as³⁰

$$\begin{aligned} H_{eff} &= PH_0P + \underbrace{PH_1P}_{1st \text{ order}} + \underbrace{PH_1RH_1P}_{2nd \text{ order}} \\ &\quad + \underbrace{PH_1RH_1RH_1P - PH_1RRH_1PH_1P}_{3rd \text{ order}} \\ &\quad + O(\Delta^4), \end{aligned} \quad (12)$$

where

$$P = \sum_a |\psi_a\rangle\langle\psi_a| \quad (13)$$

is the projection operator onto the model space in terms of the above constructed basis states $|\psi_a\rangle$, and

$$R = \sum_b \frac{|\psi_b\rangle\langle\psi_b|}{E_0 - E_0^b} \quad (14)$$

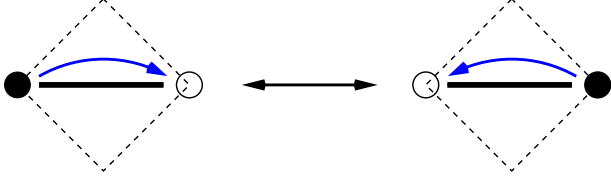


FIG. 10: (Color online) Spin exchange processes contributing to the effective Hamiltonian $H_{eff}^{(1)}$ in first order perturbation theory. Full (open) circles denote spin up (down) states.

is the resolvent operator with $E_0 = -NJ'/8$ the degenerate ground state energy of H_0 , and $E_0^b = \langle \psi_b | H_0 | \psi_b \rangle$ the energy of the basis state $|\psi_b\rangle$ of the orthogonal space O . We start by considering the first order contribution to H_{eff} . The only possible process in this case is a single spin-flip along a diagonal bond, graphically represented in Fig. 10. In terms of effective spin operators \tilde{S}_d^+ , \tilde{S}_d^- and \tilde{S}_d^z , that act on the effective dimer spin states $|\uparrow\rangle_d, |\downarrow\rangle_d$, the effective Hamiltonian in first order perturbation thus reads,

$$H_{eff}^{(1)} = -\frac{\Delta J'}{2} \sum_d (\tilde{S}_d^+ + \tilde{S}_d^-) = -\Delta J' \sum_d \tilde{S}_d^x, \quad (15)$$

corresponding to a uniform transverse magnetic field acting on the effective dimer spins. The lowest-energy eigenstate of H_{eff} for $\Delta > 0$ is the direct product state

$$|\psi_D\rangle = \bigotimes_d \frac{1}{\sqrt{2}} (|\uparrow\rangle_d + |\downarrow\rangle_d) = \bigotimes_d \frac{1}{\sqrt{2}} (|\uparrow\downarrow\rangle + |\downarrow\uparrow\rangle)_d,$$

referred to already in Eq. (5) of Sec. III, corresponding to the decoupled dimer state with each dimer forming a $S_{tot}^z = 0$ triplet state. In case of an antiferromagnetic transverse exchange, $\Delta < 0$, the lowest energy state of H_{eff} is the dimer singlet state

$$|\psi_S\rangle = \bigotimes_d \frac{1}{\sqrt{2}} (|\uparrow\rangle_d - |\downarrow\rangle_d) = \bigotimes_d \frac{1}{\sqrt{2}} (|\uparrow\downarrow\rangle - |\downarrow\uparrow\rangle)_d,$$

proven to be an exact eigenstate of the full Hamiltonian H for $\Delta < 0$ by Shastry and Sutherland⁴. However, $|\psi_D\rangle$ is not an eigenstate of the full Hamiltonian, and correlations between the effective dimer spins are introduced in higher order perturbation theory.

In order to assess the nature of these correlations, we consider processes occurring in second order perturbation theory. These involve two spin exchanges along axial bonds. Apart from diagonal terms, the result of such processes is again to flip the effective spin on one of the dimers, as shown in Fig. 11. The matrix element of each such process depends in detail on the specific local spin configuration on the dimers neighboring the dimer that undergoes the spin flip. Among the various possibilities, one with the largest amplitude is shown in Fig. 11 (a). In

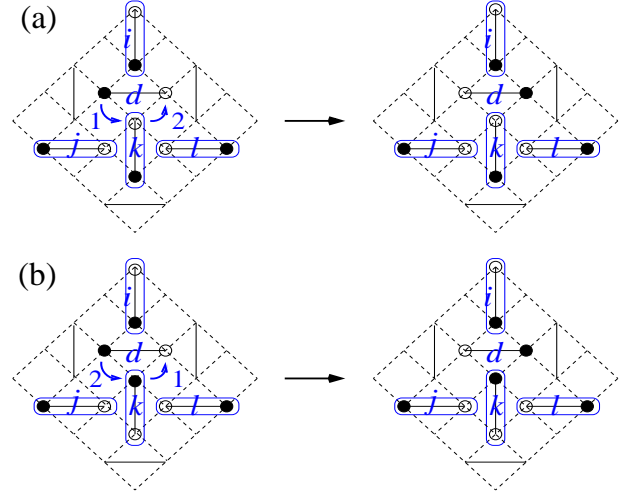


FIG. 11: (Color online) Two different spin exchange processes contributing to the effective Hamiltonian $H_{eff}^{(2)}$ in second order perturbation theory. These processes mediate the formation of an $S_{tot}^z = 0$ triplet state on the corresponding dimer, while blocking its formation on the neighboring dimers (inside ellipses). Full (open) circles denote spin up (down) states. Numbers indicate the order of the spin exchange in the processes.

the second order effective Hamiltonian $H_{eff}^{(2)}$, this process contributes a term

$$\frac{2(\Delta J)^2}{2J - J'} \tilde{S}_d^x \left(\frac{1}{2} - \tilde{S}_i^z\right) \left(\frac{1}{2} - \tilde{S}_j^z\right) \left(\frac{1}{2} - \tilde{S}_k^z\right) \left(\frac{1}{2} + \tilde{S}_l^z\right), \quad (16)$$

which provides a further contribution to the transverse field operator at site d , dressed by diagonal operators from the neighboring dimers, that project out the specific configuration of dimer spin states according to the configuration shown in Fig. 11. While the transverse field in $H_{eff}^{(1)}$ acts locally on each dimer, the dressed transverse field operators deriving from $H_{eff}^{(2)}$ lead to correlations among nearest neighbor dimer spins. For example, the spin exchange process on dimer d shown in Fig. 11 (a) could not take place as indicated by the arrows, if dimer k was in the opposite spin state. Instead, a different process could take place, as shown in Fig. 11 (b), that leads to a similar term in $H_{eff}^{(2)}$, but with a different energy denominator than in Eq. (16). In this way, details of the local dimer configuration enter the effective Hamiltonian in a rather complex manner.

The explicit form of the total effective Hamiltonian up to second order in Δ involves several terms, containing products of up to five effective spin operators, such as the term given explicitly in Eq. (16). While the ground state of this effective Hamiltonian is not directly accessible, the general structure of these terms indicate that it will be a dressed version of $|\psi_D\rangle$, with local inter-dimer correlations induced by the above virtual spin exchange processes. This reflects the QMC result, that the true ground state is close in energy to $|\psi_D\rangle$, and does not

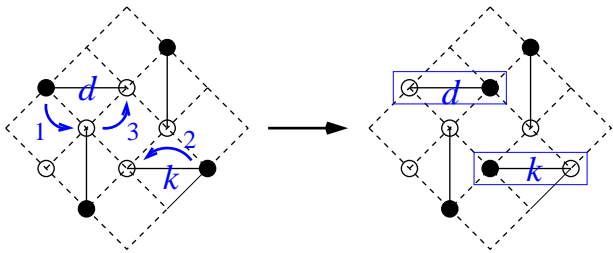


FIG. 12: (Color online) Spin exchange process contributing to the effective Hamiltonian $H_{eff}^{(3)}$ in third order perturbation theory. This process leads to a flip of the effective spins on two neighboring dimers (inside boxes). As a result of this process, the effective spins inside the boxes have been exchanged. Full (open) circles denote spin up (down) states. Numbers indicate the order of the spin exchange processes.

exhibit long ranged correlations.

The effective Hamiltonian up to second order in perturbation theory does not include transverse spin exchange terms, that would contain products of off-diagonal effective spin operators such as $\tilde{S}_d^+ \tilde{S}_k^- + \tilde{S}_d^- \tilde{S}_k^+$ on two neighboring dimers d and k . However, such terms appear in third order of the degenerate perturbation theory, e.g. from the process shown in Fig. 12. Similar to the transverse magnetic field operator in second order, the matrix elements depend on the details of the spin configuration on the neighbors of the two dimers that undergo an effective spin exchange. The transverse effective spin exchange operators are thus similarly dressed by additional projection operators. Becoming more relevant at large values of Δ , we expect that such exchange terms eventually drive the transition from the dimer triplet phase to the superfluid region, that was observed in the QMC simulations (c.f. Fig. 3).

We now turn to the special point $J' = 2J$, where the ground state in the Ising limit has an enhanced degeneracy, as discussed in Sec. II. Consider one of the J' -dimer of the Shastry-Sutherland lattice in the Ising limit $\Delta = 0$. For $J' = 2J$, this dimer can be either in one of the local configurations of Fig. 2 (a), which are also allowed configurations for $J' > 2J$, or it is part of one of the local configurations shown in Fig. 2 (b). Introducing a finite $\Delta > 0$ in first order perturbation theory, a splitting in the energy between the configurations of Fig. 2 (a) and those of Fig. 2 (b) results, since the configurations of Fig. 2 (b) cannot gain exchange energy by a transverse spin exchange along the dominant J' bonds, in contrast to the configurations of Fig. 2 (a). To first order in Δ , this energy difference equals

$$\delta E = -J + \frac{J'}{2} + \frac{\Delta J'}{2}, \quad (17)$$

near the point $(\Delta, J'/J) = (0, 2)$. A finite $\delta E > 0$ thus leads to a partial lifting of the ground state degeneracy, and only the local configurations of Fig. 2 (a) remain to span the low-energy sector. The configurations of Fig. 2

(b) are split-off by a finite energy difference $\delta E > 0$ from the ground state manifold. Since this energy difference remains positive for

$$\delta E > 0 \iff \frac{J'}{J} > \frac{2}{1 + \Delta} \quad (18)$$

we expect that as long as $J'/J \gtrsim 2/(1 + \Delta)$ close to $(\Delta, J'/J) = (0, 2)$, the system is driven by quantum effects towards the same phase as for $J' > 2J$. In fact, this expectation is in agreement with the QMC phase diagram of Fig. 3, where we found that (i) for small $\Delta > 0$ at $J' = 2J$, the system enters the dimer triplet state as it does for $J' > 2J$, and (ii) the phase boundary of the dimer triplet phase closely follows the limiting line $J'/J = 2/(1 + \Delta)$ according to $\delta E = 0$ for small Δ (compare to the dashed-dotted line in Fig. 3). The above argument was based on energy considerations on an isolated dimer. Due to this restriction, we are not able here to discern, if the superfluid phase indeed terminates at a small, but finite values of Δ , or if it persists down to any finite value of $\Delta > 0$. This would require the intra-dimer exchanges to be taken into account within higher orders of perturbation theory. However, from our analysis of the case $J' > 2J$ discussed above, we expect that also in this case, the effective model will not allow for an explicit solution, thus leaving this question unanswered. Hence, here we do not attempt to extend on this issue, but instead move on to study the magnetization process in the model under consideration.

V. MAGNETIZATION PROCESS

After exploring the ground state phase diagram, we now consider the model of Eq. (1) in the presence of a finite magnetic field h , which couples to the spins by the standard Zeeman term,

$$H \rightarrow H - h \sum_i S_i^z. \quad (19)$$

From considering a singly flipped spin with respect to the fully polarized state, one finds that the system is fully polarized for magnetic fields h beyond

$$h_s = (2J + J'/2)(1 + \Delta). \quad (20)$$

Before discussing the magnetization process of the full quantum model, it is again useful to consider first the Ising limit. The authors of Ref. 9 state that the Ising model on the Shastry-Sutherland lattice exhibits a magnetization process with a single plateau at $m/m_s = 1/2$, where m denotes the magnetization, and m_s its saturation value, at least for $J' < 2J$. In our notation, this $1/2$ plateau should extend between $2J - J'/2 < h < 2J + J'/2$. In particular, in case $J' = J$, well within the Néel ordered zero-field regime, this range becomes $3/2 < h/J < 5/2$. This conclusion in Ref. 9 was based

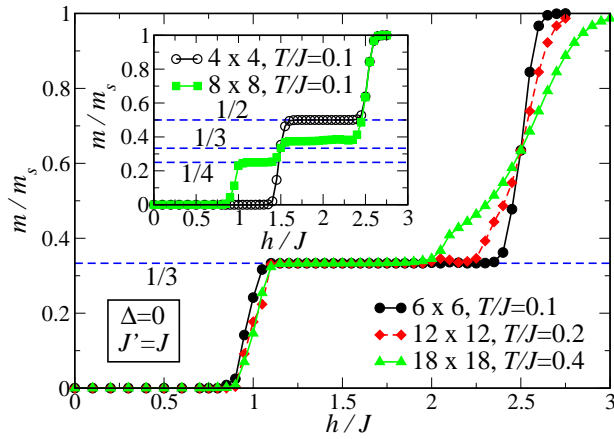


FIG. 13: (Color online) Magnetization curves m/m_s as functions of h for the Ising model on the Shastry-Sutherland lattice at $J' = J$ for different system sizes, obtained from Monte Carlo simulations. The inset shows the results for the 4×4 and 8×8 lattices.

on analyzing a finite system with 16 spins only. In order to check this conclusion on larger system sizes, we performed a systematic finite size analysis, using classical Monte Carlo (MC) simulations on lattices with up to 18×18 spins in the canonical ensemble. For these simulations, we employed a single spin-flip Metropolis algorithm, and allowed for a simulated annealing of the system from a large initial temperature $T \approx J$ down to the final temperature during an initial state of equilibration. This way we were able to obtain MC results down to $T/J = 0.1$ for $L = 4, 6$, and $T/J = 0.4$ for $L = 18$. While for the purpose of the current study, one can draw relevant conclusions on the magnetization process from these data, it will be interesting to obtain more refined numerical data on the magnetization process in the Ising limit, using extended ensemble sampling methods, similar to the approach taken in Ref. 31 for the square and triangular lattice. However, this lies beyond the scope of the current study, which is directed towards the quantum regime.

Upon presenting the MC results, we first discuss the case $J' = J$ considered in Ref. 9. Our MC data for the magnetization process on different lattices are collected in Fig. 13. The inset of Fig. 13 shows our data for a 4×4 system, which appear to confirm the conclusion of Ref. 9. However, upon increasing the system size, we find that different plateau structures appear. In general, in order to allow a system to establish a certain magnetization plateau, appropriate lattice sizes and boundary conditions must be chosen. Otherwise, geometric constraints could frustrate certain magnetization patterns. In the present case, it can be seen from the numerical data, that only for L a multiple of 3, the system establishes a wide $m/m_s = 1/3$ plateau, which is consistently observed for $L = 6, 12$ and 18 . Instead, the $L = 4$ and 8 systems cannot establish the corresponding magnetic superstructure, and hence lead to rather different magne-

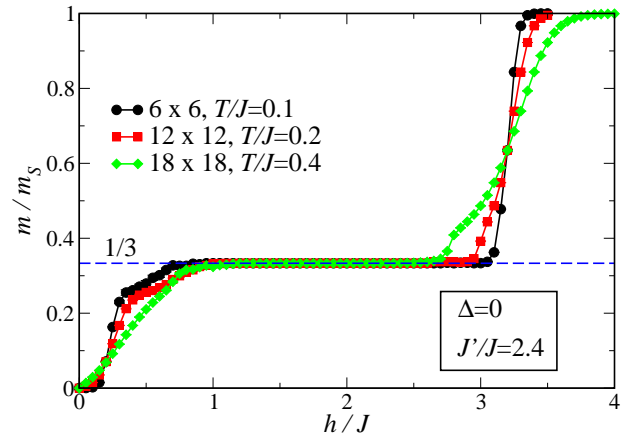


FIG. 14: (Color online) Magnetization curves m/m_s as functions of h for the Ising model on the Shastry-Sutherland lattice at $J' = 2.4J$ for different system sizes, obtained from Monte Carlo simulations.

tization curves with strong finite size effects, that do not represent thermodynamic limit behavior. The magnetization curve in Fig. 13 for $L = 6$, taken at $T/J = 0.1$, exhibits a magnetization plateau at $m/m_s = 1/3$, extending from $h = J$ up to the saturation field at $h = 5/2J$. The data shown for the two larger systems, for which higher temperatures had to be taken in the MC simulations, are consistent with a thermal smothering of the magnetization jumps out of the plateau towards $m = 0$ and full saturation, respectively. We conclude that for $J' = J$ the Ising model exhibits a single intermediate magnetization plateau at $m/m_s = 1/3$, extending from $h = J$ up to the saturation field at $h = 5/2J$. The different conclusion of Ref. 9 appears to be due to the usage of inappropriate finite lattice sizes. Note, that all values of L considered here were even, i.e. a plateau at $m/m_s = 1/2$, if it would exist in this model, would not be frustrated by finite lattice effects. In fact, as discussed below, we find that such a $1/2$ plateau appears for finite values of Δ due to quantum effects. Next, we consider the case $J' = 2.4J$, well inside the degenerate region of $J' > 2J$. Below, we will compare the Ising model result to QMC data on the magnetization process for finite $\Delta > 0$ at the same value of J'/J . The MC results for the magnetization process in the Ising limit are shown in Fig. 14, where we now consider linear system sizes L that are a multiple of 6. Again, we observe a wide $1/3$ magnetization plateau, which extends from $h \approx 0.8J$ up to the saturation field at $h = h_s = 3.2J$. A precise estimate of the lower boundary of the plateau is not accessible from the current finite size data, as we could not collect data at sufficiently low temperatures on larger systems. There appears however a finite magnetization with a smooth increase well before the plateau is entered. It will be interesting to explore this low- m regime in more detail using extended ensemble methods. The point that is important for the following discussion, and which follows also from the current MC data, is the absence again

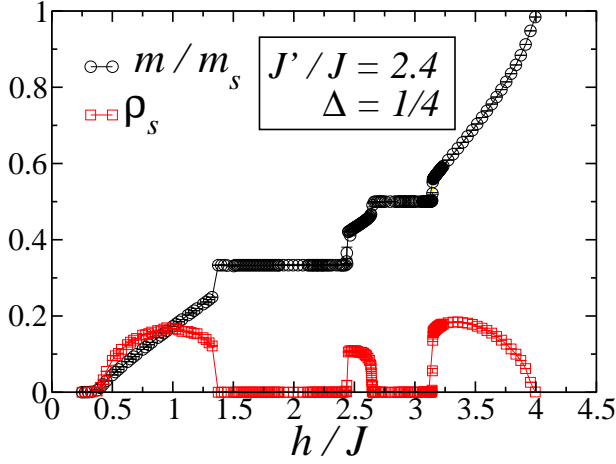


FIG. 15: (Color online) Magnetization m/m_s and spin stiffness ρ_s for $J' = 2.4J$ and $\Delta = 1/4$ as functions of the applied magnetic field h .

of a magnetization plateau at $m/m_s = 1/2$. Instead, the magnetization exhibits a jump from the $1/3$ plateau up to magnetic saturation at $h = h_s$.

As we show next, a plateau at $m/m_s = 1/2$, while not obtained in the Ising limit, emerges in the quantum model at finite values of $\Delta > 0$. Fig. 15 shows the magnetization process for $J' = 2.4J$ and $\Delta = 1/4$ from QMC simulations. We again find a magnetization plateau at $m/m_s = 1/3$ as well as a plateau at $m/m_s = 1/2$. Adding a transverse exchange to the Ising model thus leads to a softening of the large magnetization jump from $m/m_s = 1/3$ to 1 in the Ising limit, and an additional plateau region appears with $m/m_s = 1/2$. In hard-core bosonic language, the transverse exchange maps onto a non-frustrating hopping amplitude. In the current situation, this finite boson hopping does not lead always to superfluidity, but drives the system into an insulating phase at filling $\rho = 3/4$, corresponding to $m/m_s = 1/2$ (due to particle-hole symmetry, a similar insulating region emerges also for $\rho = 1/4$, corresponding to $m/m_s = -1/2$). Indeed, we find from Fig. 15, that the spin stiffness ρ_s vanishes inside both plateau regions. It is then in order to study, if the magnetic excitations in both plateau phases form period crystals, and what the structures of such solid arrays would be. Long-range crystalline ordering of magnetic excitations inside magnetic plateau regions has previously been analyzed for the isotropic spin-1/2 Heisenberg model on the Shastry-Sutherland model^{5,32,33,34,35,36,37,38}, based on different approximative schemes. The relevant structures expected from these studies are shown in the inset of Fig. 16 for the $1/3$ (upper panel), and the $1/2$ (lower panel) plateau, respectively. They are expressed in terms of periodic arrangements of $S_{tot}^z = 1$ dimer triplet states $|\uparrow\uparrow\rangle_d$, denoted by dumbbells, in a background of less polarized, e.g. $S_{tot}^z = 0$ states on the remaining dimers. We now assess, if these crystalline patterns appear also in the

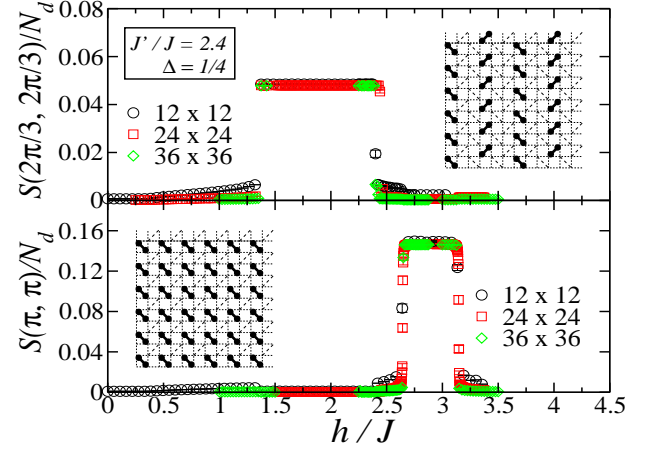


FIG. 16: (Color online) Dimer super structure factors $S(2\pi/3, 2\pi/3)$ (upper panel) and $S(\pi, \pi)$ (lower panel) at $J' = 2.4J$ and $\Delta = 1/4$ as functions of the applied magnetic field h . The insets illustrate the corresponding magnetic superstructures, where a dumbbell denotes a fully polarized dimer. $N_d = N/2$ is the number of dimers.

current quantum model, which represents an anisotropic version of the Heisenberg model considered thus far.

In a QMC simulation, one can probe exactly for these magnetic superstructures by measuring an appropriate structure factor. Hence, we analyze the ordering pattern of the magnetic excitations by measuring the triplet excitation structure factor

$$S(\mathbf{q}) = \frac{1}{N_d} \sum_{d,k} e^{i\mathbf{q}(\mathbf{r}_d - \mathbf{r}_k)} \langle P_d P_k \rangle, \quad (21)$$

where P_d is a projector on the $S_{tot}^z = 1$ dimer triplet state $|\uparrow\uparrow\rangle_d$ on dimer d . $N_d = N/2$ equals the number of dimers in the finite system of N sites. The positions \mathbf{r}_d of the dimers and the momentum space vector \mathbf{q} are defined with respect to the convenient coordinate system formed by the square lattice of dimers, with the distance between the centers of two neighboring dimers taken as unity. In this way, the solid order shown in the upper panel of Fig. 16 for $m/m_s = 1/3$ corresponds to a peak in $S(\mathbf{q}) \propto N_d$ at $\mathbf{q} = (2\pi/3, 2\pi/3)$, and at $\mathbf{q} = (\pi, \pi)$ for the order shown in the lower panel of Fig. 16 for $m/m_s = 1/2$. The main panels of Fig. 16 show these components of the structure factor for different system sizes, respectively. We checked, that no other signal in $S(\mathbf{q})$ appeared, apart from those explicitly shown. From these data we conclude, that indeed the crystalline orders of the magnetic excitations shown in Fig. 16 are stabilized within the two magnetization plateau regions, respectively. In order to study the real-space distribution of the magnetization among the lattice sites in more detail, we also measured the mean local values of the magnetization. The obtained distributions of the local magnetization are shown for the $1/3$ and $1/2$ plateau in Fig. 17 (a) and (b), respectively. They agree well with the distributions reported for the isotropic Heisenberg model

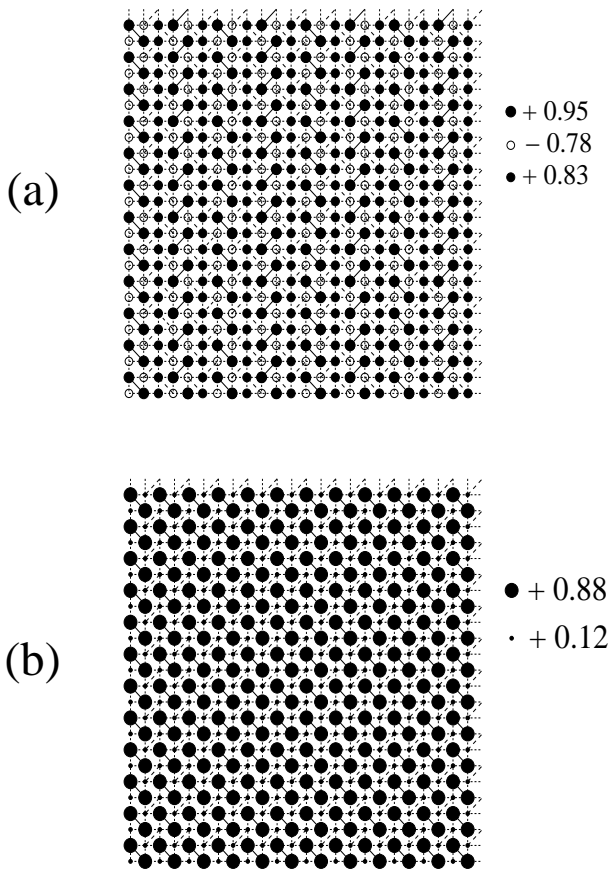


FIG. 17: (Color online) Distribution of the local magnetization m_i/m_s for the magnetization plateaus at $m/m_s = 1/3$ (a) and $1/2$ (b), represented as indicated by the size of circles on the lattice sites. Results are shown for a 24×24 lattice.

in the studies mentioned above.

Upon varying h beyond these wide magnetization plateaus, the magnetization undergoes discontinuous jumps, as seen in Fig. 15, alert when entering the $1/2$ plateau from below, where such a jump appears not that well resolved. The spin stiffness ρ_s exhibits a similar behavior, with clear jumps upon entering the plateaus, expect when entering the $1/2$ plateau from below. Apart from this case, the superfluid-insulator transitions are thus clearly first order. Concerning the region below the $1/2$ plateau, one might instead consider the presence of a supersolid state of magnetic excitations, with both a finite superfluid density and a crystalline superstructure. In order to assess, if supersolid behavior is indeed present in this regime, we show in Fig. 18 the finite size scaling of both the superfluid density ρ_s and the relevant structure factors from the neighboring magnetization plateaus at a magnetic field of $h = 2.6$, inside the possibly supersolid region. From the finite size scaling we can exclude the presence of a supersolid phase in this parameter regime. Between the two magnetization plateaus, the system is thus in a uniform superfluid state. Our analysis of the magnetization process at $J'/J = 2.4$ and $\Delta = 1/4$ did

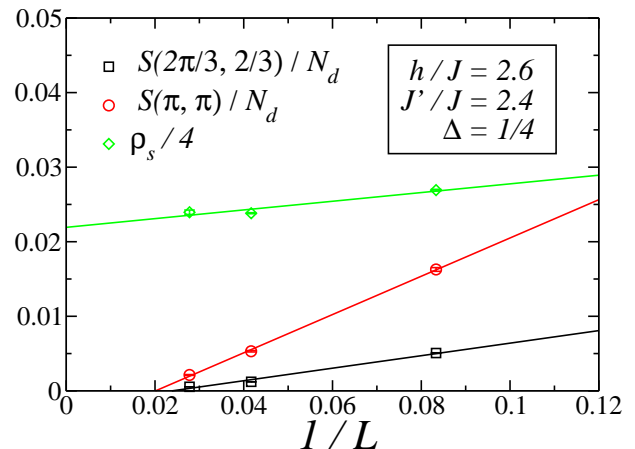


FIG. 18: (Color online) Finite size scaling of the superfluid density ρ_s and the dimer superstructure factors of the neighboring plateaus at $h = 2.6$ for $J' = 2.4J$ and $\Delta = 1/4$.

not exhibit the presence of any additional plateaus at lower values of m . Indeed, at low- m the magnetization curve as well as the superfluid density appear smooth in Fig. 15. In particular, we did not find any of the fractional magnetization plateaus mentioned in Sec. I for the compounds $\text{SrCuB}_2(\text{BO}_3)_2$ and TmB_4 , nor those found for the isotropic spin-1/2 Heisenberg model on the Shastry-Sutherland model in recent studies^{5,32,33}. We postpone a discuss on this issue to the concluding section.

Finally, we present our results for the magnetization process upon varying over a wider range of parameters space. The results of QMC simulations similar to those discussed in detail above are summarized in Fig. 19, which shows the magnetic phase diagram for a generic fixed ratio of $J'/J = 2.4$. The figure shows both the $m/m_s = 1/3$ magnetization lobe that extends from the Ising limit up to $\Delta = 0.32(2)$, as well as the emergent $m/m_s = 1/2$ lobe, that extends up to a similar value of Δ , but shrinks upon approaching the Ising limit, where no $1/2$ plateau persists.

VI. CONCLUSIONS

We studied the ground state phase diagram and the magnetization process of the spin-1/2 easy-axis XXZ model of Eq. (1) with ferromagnetic transverse spin exchange on the Shastry-Sutherland lattice. The model exhibits a Néel ordered phase for small values of J'/J and Δ , and a superfluid phase for dominant Δ . For sufficiently large values of J'/J , a dimerized phase with the dominant formation of $S_{tot}^z = 0$ triplet states on the J' -dimer bonds is stabilized, that connects to the degenerate phase of the model in the Ising limit. We like to compare this findings to the case of the isotropic Heisenberg model on the same lattice. Also in this model there is strong evidence for an intermediate phase³, separating the Néel

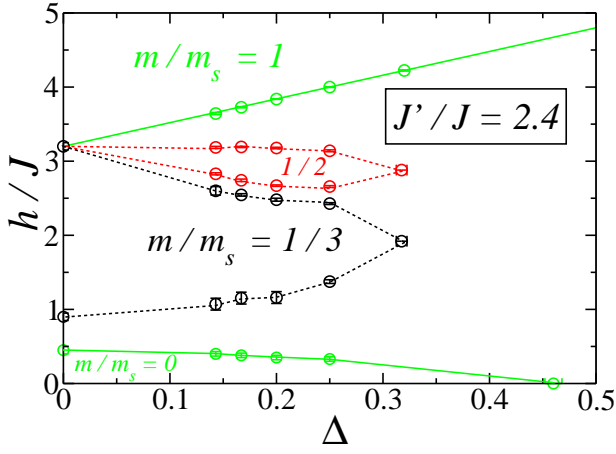


FIG. 19: (Color online) Magnetic phase diagram of the spin-1/2 XXZ model on the Shastry-Sutherland lattice with ferromagnetic transverse spin exchange at $J'/J = 2.4$ depending on the anisotropy Δ and the applied magnetic field h .

ordered phase from the dimer singlet phase. In contrast, this intermediate phase is however not a superfluid, but appears to realize a valence bond crystal driven by the frustrated nature of the transverse exchange interactions in this region²⁴.

Using classical Monte Carlo simulations to assess the magnetization process in the Ising limit, we found in contrast to previous claims⁹ no magnetization plateau at 1/2 of full saturation, but instead a 1/3 plateau, with a jump towards full saturation. The quantum model shows the presence of a 1/2 plateau in addition to the 1/3 plateau. This emergence of a magnetization plateau upon adding quantum fluctuations (via a finite Δ) to the Ising model remains of the previously observed emergence of a magnetization plateau via thermal fluctuations in the classical Heisenberg model on the kagome lattice³⁹. While we examined the case of a ferromagnetic transverse spin exchange, the experimental observation of a 1/2 plateau in the compounds TmB_4 and $\text{SrCuB}_2(\text{BO}_3)_2$ can be taken as indication, that such a plateau also emerges for antifer-

romagnetic transverse exchange. Indeed, a 1/2 plateau is consistently reported also in the studies on the magnetization process of the isotropic Heisenberg model on the Shastry-Sutherland lattice³.

With respect to other reported magnetization plateaus both from experiments and in recent theoretical work, we did not obtain evidence from our quantum Monte Carlo simulations, that they are stabilized in the current model. In particular, the pronounced 1/6 plateau, consistently reported in recent theoretical work^{5,32,33}, has not been found for the parameter region we examined in our simulations (we performed various scans inside the range $2 < J'/J < 3$, down to $\Delta = 1/7$, with results similar to those presented in detail above), even though the proposed magnetic unit cell^{5,32,33} is commensurate with the finite lattices that we employed in our simulations. We explicitly checked that no signal in the relevant component of $S(\mathbf{q})$ at $\mathbf{q} = (\pi, \pi/3)$ appears near $m/m_s = 1/6$ in this model. Hence, we conclude that the model considered here exhibits magnetization plateaus at 1/2 and 1/3 of the full saturation, only. Future work could explore in more detail the magnetization process in the Ising model inside the low-field region using extended ensemble methods, similar to the approach taken in Ref. 31. It would be interesting to apply the theoretical approaches employed in Refs. 32 and 33 to the current model, in order to to check their predictions against the unbiased large-scale quantum Monte Carlo results present here.

Acknowledgments

We thank A. Läuchli, F. Mila, R. Mössner, A. Muramatsu and D. Poilblanc for useful discussions. Financial support by the Deutsche Forschungsgemeinschaft under Grant No. WE 3649/2-1 and through SFB/TR 21 is gratefully acknowledged, as well as the allocation of CPU time by HLRS Stuttgart and NIC Jülich. The employed numerical simulation code was partially based on the ALPS libraries⁴⁰.

- ¹ M. Tamura, A. Nakao, and R. Kato, J. Phys. Soc. Jpn. **75**, 093701 (2006).
- ² S.-H. Lee, H. Kikuchi, Y. Qiu, B. Lake, Q. Huang, K. Habicht, and K. Kiefer, Nature Materials **6**, 853 (2007).
- ³ S. Miyahara and K. Ueda, J. Phys.: Condens. Matter **15**, R327 (2003); and references therein.
- ⁴ B. S. Shastry and B. Sutherland, Physica (Amsterdam) **108B**, 1069 (1981).
- ⁵ S. E. Sebastian, N. Harrison, P. Sengupta, C. D. Batista, S. Francoual, E. Palm, T. Murphy, H. A. Dabkowska, and B. D. Gaulin, arXiv:0707.2075 (2007).
- ⁶ F. Levy, I. Sheikin, C. Berthier, M. Horvatic, M. Takigawa, H. Kageyama, T. Waki, and Y. Ueda, Europhys. Lett. **81**, 67004 (2008).

- ⁷ M. Takigawa, S. Matsubara, M. Horvatic, C. Berthier, H. Kageyama, and Y. Ueda, arXiv:0710.5216 (2007).
- ⁸ S. Gabani, S. Matas, P. Priputen, K. Flachbart, K. Siemensmeyer, E. Wulf, A. Evdokimova, and N. Shitsevalova, arXiv:0712.0519 (2007).
- ⁹ K. Siemensmeyer, E. Wulf, H.-J. Mikeska, K. Flachbart, S. Gabani, S. Matas, P. Priputen, A. Evdokimova, and N. Shitsevalova, arXiv:0712.1537 (2007).
- ¹⁰ M. Troyer and U.-J. Wiese, Phys. Rev. Lett. **94**, 170201 (2005).
- ¹¹ S. R. White and A. L. Chernyshev, arXiv:0705.2746 (2007).
- ¹² H. C. Jiang, Z. Y. Weng, and D. N. Sheng, arXiv:0804.1616 (2008).
- ¹³ G. Murthy, D. Arovas, and A. Auerbach, Phys. Rev. B **55**,

- 3104 (1997).
- ¹⁴ S. Wessel and M. Troyer, Phys. Rev. Lett. **95**, 127205 (2005).
 - ¹⁵ R. Melko, A. Paramekanti, A. Burkov, A. Vishwanath, D. Sheng, and L. Balents, Phys. Rev. Lett. **95**, 127207 (2005).
 - ¹⁶ D. Heidarian and K. Damle, Phys. Rev. Lett. **95**, 127206 (2005).
 - ¹⁷ S. V. Isakov, S. Wessel, R. G. Melko, K. Sengupta, and Y. B. Kim, Phys. Rev. Lett. **97**, 147202 (2006).
 - ¹⁸ K. Damle and T. Senthil, Phys. Rev. Lett. **97**, 067202 (2006).
 - ¹⁹ L. Balents, M. P. A. Fisher, and S. M. Girvin, Phys. Rev. B **65**, 224412 (2002).
 - ²⁰ D. N. Sheng and L. Balents, Phys. Rev. Lett. **94**, 146805 (2005).
 - ²¹ S. V. Isakov, Y. B. Kim and A. Paramekanti, Phys. Rev. Lett. **97**, 207204 (2006).
 - ²² A. Banerjee, S. V. Isakov, K. Damle, and Y. B. Kim, Phys. Rev. Lett. **100**, 047208 (2008).
 - ²³ L. C. Pauling, *The Nature of the Chemical Bond and the Structure of Molecules and Crystals: an Introduction to Modern Structural Chemistry* (Cornell University Press, 20th Edition, Ithaca, New York, USA, 1986).
 - ²⁴ A. Läuchli, S. Wessel, and M. Sgrist, Phys. Rev. B **66**, 014401 (2002).
 - ²⁵ O. F. Syljuåsen and A. W. Sandvik, Phys. Rev. E **66**, 046701 (2002).
 - ²⁶ F. Alet, S. Wessel, and M. Troyer, Phys. Rev. E **71**, 036706 (2005).
 - ²⁷ A. W. Sandvik, Phys. Rev. B **59**, R14157 (1999).
 - ²⁸ E. L. Pollock and D. M. Ceperley, Phys. Rev. B. **36**, 8343 (1987).
 - ²⁹ M. Hasenbusch and T. Török, J. Phys. A **32**, 6361 (1999).
 - ³⁰ I. Lindgren, J. Phys. B: Atom. Molec. Phys. **7**, 2441 (1974).
 - ³¹ C.-O. Hwang, S.-Y. Kim, D. Kang, and J. M. Kim, J. Stat. Mech. L05001 (2007).
 - ³² J. Dorier, K. P. Schmidt, and F. Mila, arXiv:0806.3406 (2008).
 - ³³ A. Abendschein and S. Capponi, arXiv:0807.1071 (2008).
 - ³⁴ T. Momoi and K. Totsuka, Phys. Rev. B **61**, 3231 (2000).
 - ³⁵ T. Momoi and K. Totsuka, Phys. Rev. B **62**, 15067 (2000).
 - ³⁶ S. Miyahara, F. Becca, and F. Mila, Phys. Rev. B **68**, 024401 (2003).
 - ³⁷ S. Miyahara and K. Ueda, Phys. Rev. B **61**, 3417 (2000).
 - ³⁸ G. Misguich, T. Jolicoeur, and S. M. Girvin, Phys. Rev. Lett. **87**, 097203 (2001).
 - ³⁹ M. E. Zhitomirsky, Phys. Rev. Lett. **88**, 572041 .
 - ⁴⁰ F. Albuquerque et al. (ALPS Collaboration), J. Magn. Mater. **310**, 1187 (2007).